

# Salt-assisted construction of hydrophilic carbon nitride photocatalysts with abundant water molecular adsorption sites for efficient hydrogen production



Chong Wang <sup>a,1</sup>, Yichun Lu <sup>b,1</sup>, Zequn Wang <sup>c</sup>, Hongwu Liao <sup>a</sup>, Weiming Zhou <sup>a,\*</sup>, Yuhe He <sup>b</sup>, Sameh M. Osman <sup>d</sup>, Meng An <sup>c,\*</sup>, Yusuke Asakura <sup>e</sup>, Yusuke Yamauchi <sup>e,f,g</sup>, Liwei Wang <sup>h,\*</sup>, Zhanhui Yuan <sup>a,\*</sup>

<sup>a</sup> College of Materials Engineering, Fujian Agriculture and Forestry University, Fuzhou 350002, China

<sup>b</sup> School of Energy and Environment and State Key Laboratory of Marine Pollution, City University of Hong Kong, Kowloon Tong, Hong Kong SAR, China

<sup>c</sup> College of Mechanical and Electrical Engineering, Shaanxi University of Science and Technology, Xi'an 710021, China

<sup>d</sup> Chemistry Department, College of Science, King Saud University, P.O. Box 2455, Riyadh 11451, Saudi Arabia

<sup>e</sup> Department of Materials Process Engineering, Graduate School of Engineering, Nagoya University, Nagoya 464-8603, Japan

<sup>f</sup> School of Chemical Engineering and Australian Institute for Bioengineering and Nanotechnology (AIBN), The University of Queensland, Brisbane, QLD 4072, Australia

<sup>g</sup> Department of Chemical and Biomolecular Engineering, Yonsei University, Seoul 03722, South Korea

<sup>h</sup> College of Materials and Chemical Engineering, Minjiang University, Fuzhou, Fujian Province 350108, China

## ARTICLE INFO

### Keywords:

Carbon nitride  
Photocatalysis  
Hydrogen production  
Hydrophilic  
Salt-assisted synthesis

## ABSTRACT

Polymer carbon nitride (PCN), as an affordable and easily prepared photocatalyst, has acquired extensive attention for hydrogen production. However, bulk carbon nitride material exhibits poor dispersibility in water due to the relatively inert surface which limits its quantum efficiency in photocatalytic hydrogen production. In this study, a hydrophilic carbon nitride (HCN) is successfully synthesized by a novel salt-assisted heating process. The heightened water adsorption capacity may contribute additional active sites conducive to the photocatalytic hydrogen production reaction. Meanwhile, potassium ion doping and material size reduction greatly enhance the charge transfer and separation ability of HCN. Consequently, HCN exhibits highly efficient photocatalytic activity for hydrogen production, achieving a rate of  $392 \mu\text{mol}\cdot\text{h}^{-1}$ , which is 16 times greater than that of pristine PCN. The simply developed synthetic strategy adopted here provides a novel concept for functionalizing carbon nitride and opening a distinct pathway for the construction of exceptionally efficient photocatalytic systems.

## 1. Introduction

Substituting fossil fuels with sustainable clean energy is a novel strategy to reduce carbon emissions and simultaneously alleviate the growing energy crisis [1–4]. The photocatalytic water splitting for hydrogen production reaction, which converts renewable and pollution-free solar energy into carbon-free hydrogen fuel, has attracted extensive attention [5–8]. Theoretically, photocatalytic hydrogen production can be carried out under mild conditions as long as the thermodynamic conditions of proton reduction are satisfied [9]. However, constructing a simple and efficient hydrogen production system in

practice is still quite challenging, as the light absorption capacity, efficiency, and durability of photocatalysts limit the further utilization of hydrogen production reactions [10–12]. Thus, discovering a highly active, low-cost, and long-lived photocatalyst is critical for the broader implementation of photocatalytic hydrogen production [13]. Moreover, designing such a type of photocatalyst requires materials that can be well dispersed in water to provide more reaction sites and have excellent charge dissociation/transfer capabilities.

Polymeric carbon nitride (PCN) has recently been demonstrated as a highly promising photocatalyst for hydrogen production, due to its elevated stability, tunable electronic structure, and ease of fabrication

\* Corresponding authors.

E-mail addresses: [zhouweiming721@126.com](mailto:zhouweiming721@126.com) (W. Zhou), [anmeng@sust.edu.cn](mailto:anmeng@sust.edu.cn) (M. An), [asa.y@nagoya-u.jp](mailto:asa.y@nagoya-u.jp) (Y. Asakura), [wlw@mju.edu.cn](mailto:wlw@mju.edu.cn) (L. Wang), [zhanhuiyuan@fafu.edu.cn](mailto:zhanhuiyuan@fafu.edu.cn) (Z. Yuan).

<sup>1</sup> These authors contributed equally: Chong Wang and Yichun Lu.

[14–16]. Generally, nitrogen-rich precursors can be directly converted into PCN through a thermal polymerization reaction [17]. The heptazine units are connected through tertiary amines to form the conjugated planes of PCN, while the layers are stacked by strong hydrogen bonding and van der Waals forces to create a bulk structure [18]. Although hydrophilic primary and secondary amine groups are evidenced to exist, the overall hydrophilicity of PCN is not ideal due to the enormous lateral sizes and the fewer edge active sites [19]. Moreover, the suboptimal photocatalytic efficiency of hydrogen production in PCN is attributed to the limited efficiency in separating photo-generated carriers.

To address the intrinsic challenge of PCN, various approaches, such as heteroatom doping, nanostructure design, and heterojunction construction, are employed to enhance photocatalytic hydrogen production efficiency [20–23]. A practical method involves increasing the dispersion of PCN in water to expose more active sites [24]. Surface functionalization and lateral size adjustment are common methods to improve the dispersion of PCN in water [25]. However, both methods involve strong acids/alkalis in the synthesis or post-treatment process, potentially damaging the PCN structure and exposing more edge active sites to improve hydrophilicity [26–28]. Furthermore, the use of strong acid/base is costly and environmentally unfriendly, limiting its more comprehensive application. Therefore, synthesizing novel carbon nitride materials with favorable hydrophilicity through more sustainable methods is challenging.

Herein, we describe a novel salt-assisted route to synthesize hydrophilic carbon nitride (HCN) using ammonium thiocyanate and potassium chloride (KCl) as precursors. Compared to bulk carbon nitride (BCN), the HCN particle size is significantly reduced and has abundant edge active sites, enabling HCN to disperse well in water to form a quasi-homogeneous system. Simultaneously, the salt-assisted process introduces potassium ions into the structure, enhancing charge separation performance. Benefiting from these optimized properties, the photocatalytic hydrogen production activity of HCN has been significantly improved compared to the pristine BCN.

## 2. Experimental section

### 2.1. Chemicals

Ammonium thiocyanate ( $\text{NH}_4\text{SCN}$ , 98.5%) and chloroplatinic acid hexahydrate ( $\text{H}_2\text{PtCl}_6 \cdot 6\text{H}_2\text{O}$ , 99%) were procured from Sinopharm Chemical Reagent. Potassium chloride (KCl, 99%) was purchased from Alfa Aesar Chemicals.

### 2.2. Catalyst synthesis

#### 2.2.1. Synthesis of BCN

$\text{NH}_4\text{SCN}$  (10 g) was transferred to a covered crucible and heated in the air to 550 °C with a rate of 6 °C·min<sup>-1</sup> for a duration of 4 hours in a muffle furnace. Subsequent to natural cooling to room temperature, the final solid catalyst (BCN) was obtained by grinding.

#### 2.2.2. Synthesis of HCN

$\text{NH}_4\text{SCN}$  (10 g) was ground with KCl (1 g) and the mixture was transferred to a covered crucible. Then, the mixture was heated in the air to 550 °C with a rate of 6 °C·min<sup>-1</sup> for 4 hours in a muffle furnace. After natural cooling to room temperature, excess KCl was removed by dialysis for 24 h. Following the complete evaporation of the water, a solid product (HCN) was obtained.

#### 2.2.3. Synthesis of HCN solution

Solid HCN (50 mg) was introduced into 100 mL of deionized water. The resulting HCN solution was obtained after 5 minutes of sonication.

### 2.3. Characterization

The chemical structure of the samples was determined employing Fourier-transform infrared spectra (Thermo IS-50), <sup>13</sup>C NMR spectra (Bruker Advance III 500 spectrometer), and X-ray photoelectron spectroscopy (Thermo ESCALAB250). The properties of HCN in water were analyzed by measuring the Zeta potential and size distribution of HCN solution (Malvern Zetasizer Nano ZS). The crystal structure of the samples was characterized through X-ray diffraction (Miniflex, Rigaku). The morphologies of the samples were scrutinized through field emission scanning electron microscopy (JSM-6700F) and transmission electron microscopy (Zeiss 912 microscope). The optical characteristics of the samples were assessed via UV-Vis diffuse reflectance spectra (PerkinElmer UV/Vis/NIR Spectrometer Lamda 950) and photoluminescence spectra (Horiba Fluorolog TCSPC spectrophotometer) and electron paramagnetic resonance (Bruker model A300 spectrometer). Microscopic and pore structure details of the sample were ascertained through nitrogen adsorption and desorption analyses (Micromeritics ASAP 2460 surface area and porosity analyzer).

### 2.4. Photocatalytic tests

#### 2.4.1. Photocatalytic hydrogen production test

50 mg of catalyst was introduced into a reactor containing 100 mL of water, supplemented with an additional 10 mL of triethanolamine. Then, the loading of 3 wt% Pt cocatalyst was conducted by directly dissolving  $\text{H}_2\text{PtCl}_6$  into the system. Simultaneously, the reaction solution underwent repeated evacuation to eliminate air completely. A 300 W xenon lamp served as the illumination source, with different cutoff filters employed to regulate the wavelength range. To maintain the reaction solution's temperature at 12 °C, circulating water was employed. The gases generated by the photocatalytic reaction were analyzed utilizing an online gas chromatography equipped with thermal conductivity detector. Argon was used as the carrier gas.

The determination of the apparent quantum yield (AQY) for the  $\text{H}_2$  production involved substituting the Xe lamp with various wavelengths of light-emitting diodes (LEDs) equipped with band-pass filters. The AQY was calculated as follows:

$$\text{AQY} = \frac{\text{The amount of reaction electrons}}{\text{The incident photons}} \times 100\% \quad (1)$$

#### 2.4.2. Photocatalytic hydrogen peroxide production test

50 mg of catalyst was introduced into a reactor containing 27 mL of water, supplemented with an additional 3 mL of isopropanol. The catalyst dispersion was achieved through ultrasonic treatment for 5 minutes, followed by bubbling  $\text{O}_2$  through the solution for 15 minutes. Subsequently, a 300 W xenon lamp served as the illumination source, with a cutoff filter employed to regulate the wavelength range. To maintain the reaction solution's temperature at 25 °C, circulating water was employed. Post-reaction, the quantity of hydrogen peroxide was ascertained through redox titration using 0.2 mM  $\text{KMnO}_4$  and the addition of 5 mL of 1 M  $\text{H}_2\text{SO}_4$  solution. Equivalence between the concentration of the  $\text{KMnO}_4$  solution and  $\text{H}_2\text{O}_2$  concentration was determined when the solution turned pink upon  $\text{KMnO}_4$  addition, and this color persisted for one minute.

### 2.5. (Photo)electrochemical measurements

(Photo)electrochemical measurements were executed by employing Ag/AgCl and platinum foil as the reference and counter electrodes, respectively. The selected electrolyte was 20 mL  $\text{Na}_2\text{SO}_4$  solution (0.2 M, pH = 6.8). The construction of working electrodes involved the dispersion of 5 mg of the sample in 0.8 mL of dimethylformamide (DMF) or  $\text{H}_2\text{O}$  through sonication to form a slurry mixture. Subsequently, 20  $\mu\text{L}$  of the slurry was drop-coated onto F-doped  $\text{SnO}_2$ -coated (FTO) glass,

and the resulting sample was air-dried to obtain the working electrode.

## 2.6. Computational method

The Vienna ab-initio Simulation Package (VASP), based on density functional theory (DFT), served as the computational framework for all calculations. Electron-ion interactions were simulated using the Projector-augmented wave (PAW) method with the GGA-PBE functional. In order to mitigate the bandgap underestimation associated with the standard GGA-PBE functional, supercells comprising 72 and 36 atoms, each with a vacuum layer of 10 Å, were selected to represent the pristine BCN and HCN models, respectively. A cut-off energy of 450 eV was uniformly applied to both supercell models, as previously specified. Structural optimization was conducted until the total energy difference per atom reached below  $1 \times 10^{-5}$  eV, and the Hellmann-Feynman forces

acting on each atom were reduced to less than  $0.01 \text{ eV} \cdot \text{\AA}^{-1}$ . For the visualization of the HOMO and LUMO orbital distributions, an isosurface value of  $0.02 \text{ e} \cdot \text{\AA}^{-3}$  was set. Consistent with previous research, phonon density of states (DOS) was acquired through self-consistent DFT total energy calculations.

The adsorption energy  $E_{\text{binding}}$  were calculated as follows:

$$E_{\text{binding}} = E_{\text{tot,mo}} - E_{\text{tot,eq}} \quad (2)$$

where  $E_{\text{tot,mo}}$  denoted the total energy of the system after the displacement of water molecules to locations 15 Å away from the BCN and HCN surfaces.  $E_{\text{tot,eq}}$  signified the total energy of the system when water molecules were positioned at equilibrium sites on the BCN and HCN surfaces. The energy of each system was computed using density functional theory (DFT) implemented in the Vienna Ab initio Simulation

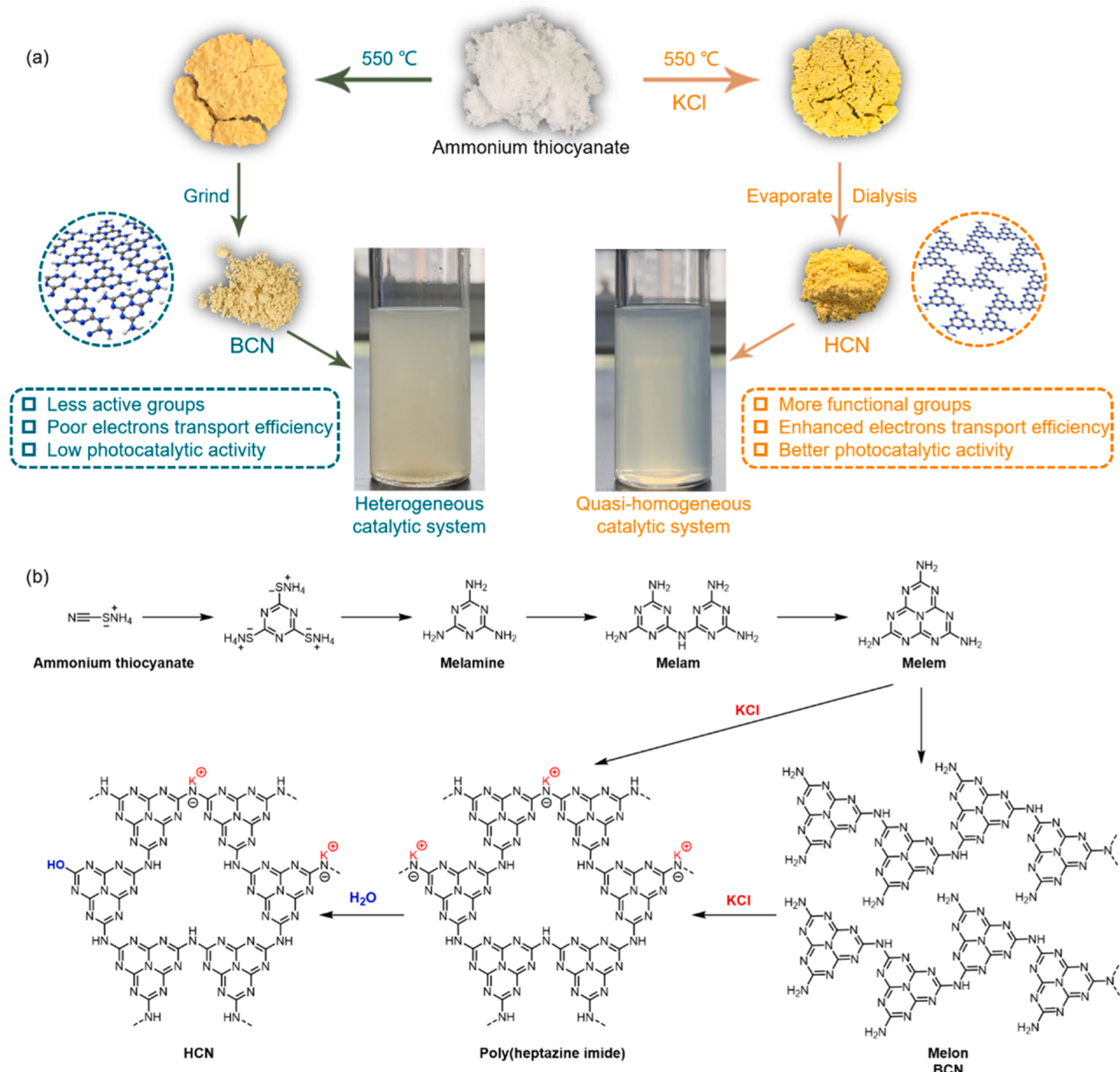


Fig. 1. (a) The synthetic route of HCN and BCN. (b) The proposed formation route of HCN and BCN.

Package (VASP) with projector augmented wave (PAW) pseudopotentials. The exchange-correlation function employed the Becke-Lee-Yang-Parr (BLYP) variant of the generalized gradient approximation (GGA). The convergence criteria for the total energy and ionic force were set  $1 \times 10^{-8}$  eV and  $0.02$  eV $\cdot\text{\AA}^{-1}$ . The plane-wave cutoff energy was established at 400 eV.

### 3. Results and discussion

#### 3.1. The evidence of catalyst hydrophilicity enhancement and potassium doping

The HCN catalyst is prepared using a salt-assisted synthetic route as illustrated in Fig. 1a. The preparation procedure for the BCN catalyst is conducted in the same manner without KCl added, and the possible synthesis process is described in Fig. 1b. To verify the chemical structure of HCN and its potential hydrophilicity, Fourier-transform infrared (FT-IR) spectroscopy is employed. As shown in Fig. 2a, both HCN and BCN samples exhibit a characteristic heptazine ring breathing vibration peak around  $810\text{ cm}^{-1}$  [29]. Additionally, broad and intense bands at  $1200\text{--}1700\text{ cm}^{-1}$  are discernible in both samples, aligning with the stretching vibrations of  $\text{C}=\text{N}$ ,  $\text{C}-\text{NH}-\text{C}$  and  $\text{N}_3\text{C}$  in the heptazine ring [30]. These results confirm the consistency of the structural units in the two samples. Notably, the extensive band spanning  $3000\text{--}3400\text{ cm}^{-1}$  in BCN is ascribed to the stretching models of the amino groups ( $-\text{NH}_x$ ), and the intensity of amino group is weakened in HCN [31]. The FT-IR spectrum of HCN also shows the vibration peak of  $-\text{NH}_x$ . However, the peak intensity is weak and therefore, not very obvious. Furthermore, a new peak appears around  $3400\text{--}3700\text{ cm}^{-1}$ , attributed to the stretching models of the hydroxyl species ( $-\text{OH}$ ) [32]. This suggests that HCN may exhibit stronger hydrophilicity. Additionally, new peaks are observed in the spectrum of HCN after salt-assisted synthesis. The terminal cyano group ( $-\text{C}\equiv\text{N}$ ) stretch is found at  $2150\text{ cm}^{-1}$ , possibly resulting from the destruction of the heptazine ring by the salt corrosion effect at high temperatures [33]. The symmetric and asymmetric vibrations of potassium- $\text{NC}_2$  groups are also evident at  $995$  and  $1150\text{ cm}^{-1}$ , indicating the

incorporation of potassium ions into the structure through the salt-assisted method [34]. The increase of hydrophilic groups on the surface of HCN is beneficial for the interaction between the catalyst and water molecules. In addition, the doping of potassium ions may affect the charge transfer performance of HCN.

The structure of the samples is further investigated using solid-state  $^{13}\text{C}$  CP-MAS NMR measurements. As shown in Fig. S1, two distinct peaks are observed in the spectrum of BCN (156.3 and 161.4 ppm), corresponding to the  $\text{CN}_3$  (C1) and  $\text{CN}_2$  (C2) in the structural unit of carbon nitride, respectively [35]. In comparison, two new  $^{13}\text{C}$  signals at 122.2 and 171.8 ppm are seen in HCN, consistent with the values for  $\text{C}\equiv\text{N}$  (C3) and the neighbor C atom (C4) (Fig. 2b) [36]. Combined with the FT-IR test results, it can be concluded that cyano groups are present in the HCN structure.

X-ray photoelectron spectroscopy (XPS) is conducted to fully determine the chemical composition of the HCN sample (Fig. S2). The high-resolution C 1 s spectrum of HCN can be resolved into three distinct peaks, 288.3 (sp<sup>2</sup>-bound carbon in the aromatic ring), 286.4 (heptazine-ring carbon next to imide bridge), and 284.8 eV (graphite carbon atoms), respectively (Fig. 2c) [37]. Notably, the peak intensity at 286.4 eV in HCN is significantly enhanced compared to BCN, indicating the presence of cyano group in the HCN structure [38]. In the high-resolution N 1 s spectrum of HCN, three peaks at 400.7, 398.6, and 399.5 eV are identified, which can be correlated to the  $\text{C}-\text{NH}_x$ ,  $\text{N}_2\text{C}$ , and  $\text{N}_3\text{C}$ , respectively (Fig. 2d) [39]. As displayed in Fig. 2e, the peak intensity of HCN at 531.7 eV (C-OH) is much higher than in BCN, suggesting that HCN may exhibit better hydrophilic and dispersive properties [40]. The K 2p XPS signals are observed at 295.7 and 292.9 eV, confirming the successful doping of the K element in the HCN frameworks (Fig. 2f). The XPS elemental analysis results show a significant increase in the K and O elements content in the sample with salt-assisted synthesis and dialysis (Table S1). Moreover, there are no apparent signals corresponding to Cl 2p (Fig. S3a) and S 2p (Fig. S3b), indicating the absence of Cl and S elements in the structure.

To examine the role of the abundant hydroxyl group on the surface of HCN, contact angle (CA) experiments are conducted. HCN exhibits a

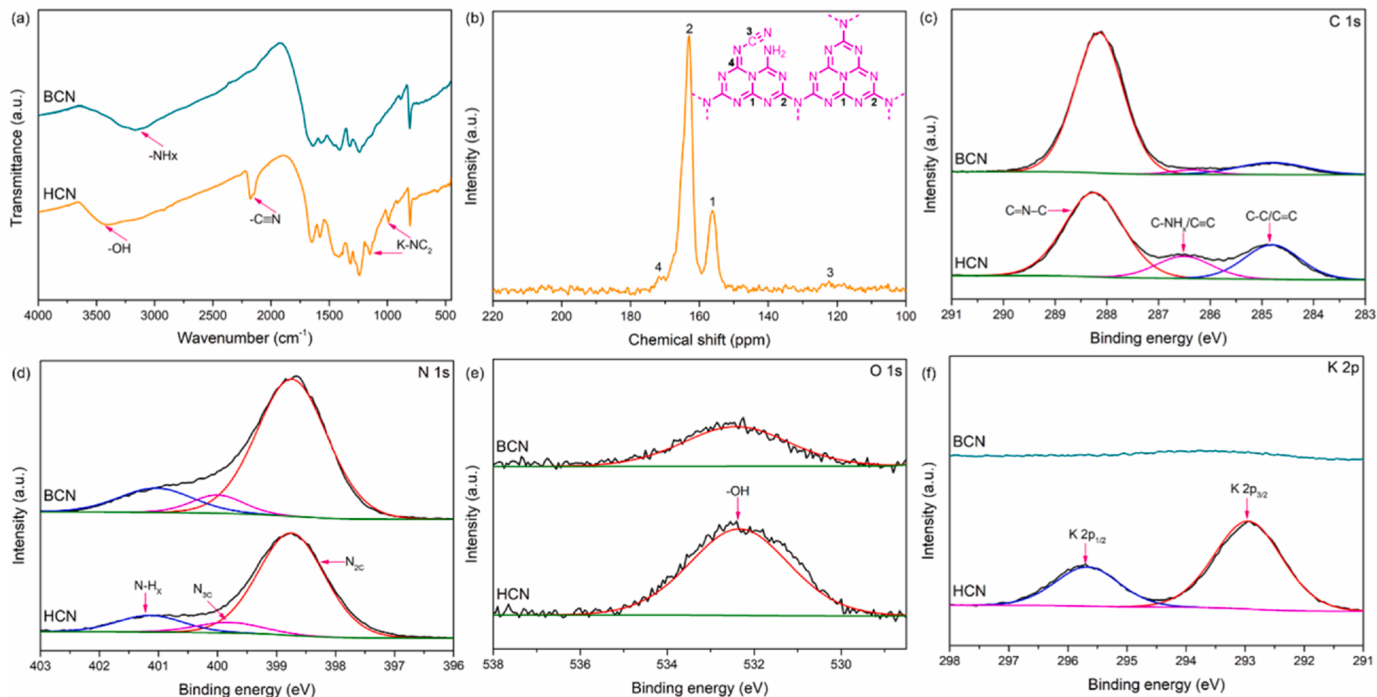


Fig. 2. (a) The FT-IR spectra of HCN and BCN. (b) Solid-state  $^{13}\text{C}$  CP-MAS NMR spectrum of HCN. The high-resolution XPS spectra of (c) C 1 s, (d) N 1 s, (e) O 2p, and (f) K 2p for HCN and BCN.

cambered water droplet with a contact angle of  $18.6^\circ$ , which is significantly lower than that of BCN ( $54.7^\circ$ ), indicating its superior hydrophilicity (Fig. 3a). Furthermore, HCN can be well dispersed in water, whereas BCN cannot form a stable dispersion under the same conditions (Fig. S4). HCN exhibits a more negative Zeta potential (-54 mV) compared to BCN (-47 mV) at pH of 7.2, indicating that the HCN solution is more stable (Fig. 3b). The particle sizes of dispersed HCN show a good Gaussian distribution with an average diameter of 290 nm (Fig. 3c). These results demonstrate that HCN can form a quasi-homogeneous photocatalytic system. In addition, when a small amount of acid is added as a trigger, a hydrogel can be formed (Fig. S5). The content of this section will be the focus of our future research work.

Salt-assisted synthesis leads to a difference in the chemical structure, resulting in the crystal structure change. As shown by X-ray diffraction (XRD), BCN exhibits two peaks situated at 13.2 and 27.3, corresponding to the (100) and (002) planes of carbon nitride, respectively (Fig. 3d) [41]. In contrast, the XRD pattern of HCN differs from that of BCN. The diffraction peaks due to periodic in-plane heptazine structures (8.1 and 9.9) of HCN are shifted to lower angles, indicating an expanded lattice after the salt-assisted synthesis, suggesting possible doping of K into the structure [42]. Moreover, the main diffraction peak of HCN attributed to the PCN layer stacking shifts to higher angles compared to BCN, suggesting a decreased layer spacing, which facilitates electron transport between layers. Additionally, the full width at half-maximum (FWHM) of the (002) plane for HCN is narrower than BCN, indicating an

improved short-range order degree of HCN (Fig. S6). Thus, it can be concluded that the salt-assisted synthesis not only changes the crystal structure of the catalyst but also introduces cyano and hydroxyl groups on the surface.

In scanning electron microscopy (SEM) image (Fig. 4a), HCN solid exhibits an irregular sheet and particle stacking, similar to the traditional BCN (Fig. S7). Subsequently, we evaporated a drop of dispersed HCN solution on the silicon wafer for scanning electron microscopy testing. It is evident that HCN is more dispersed and has a smaller particle size in water (Fig. 4b). Interestingly, further diluting the dispersed HCN solution reduces the particle size, which facilitates maximum exposure of the active sites to water (Fig. 4c). In addition, a decrease in the size of the photocatalyst will also reduce the distance of carrier migration, allowing more carriers to migrate to the surface, thereby promoting the photocatalytic reaction. In order to verify the invertibility of this phenomenon, the dispersed HCN solution was heated. As water dwindles in the system, dispersed particles and sheets gradually accumulate and eventually form large-scale lumps (Fig. S8). Due to this aggregation, the HCN solid does not display a higher surface area than BCN (Fig. S9).

The morphological and structural details of HCN are investigated by transmission electron microscopy (TEM). Several layers of irregular nanosheet stacking structures are observed in the low-magnification TEM image (Fig. 4d). The crystalline quality of the HCN solid is further visualized through the high-resolution TEM (HRTEM)

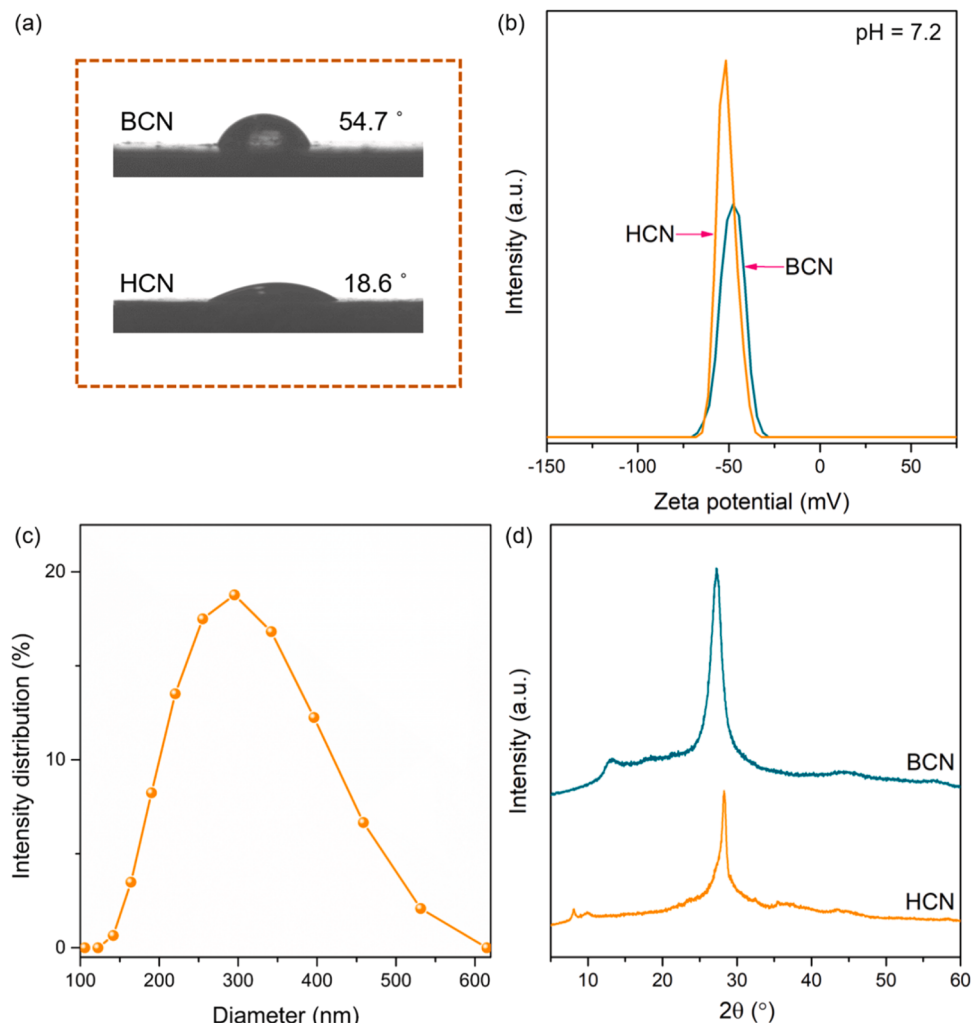
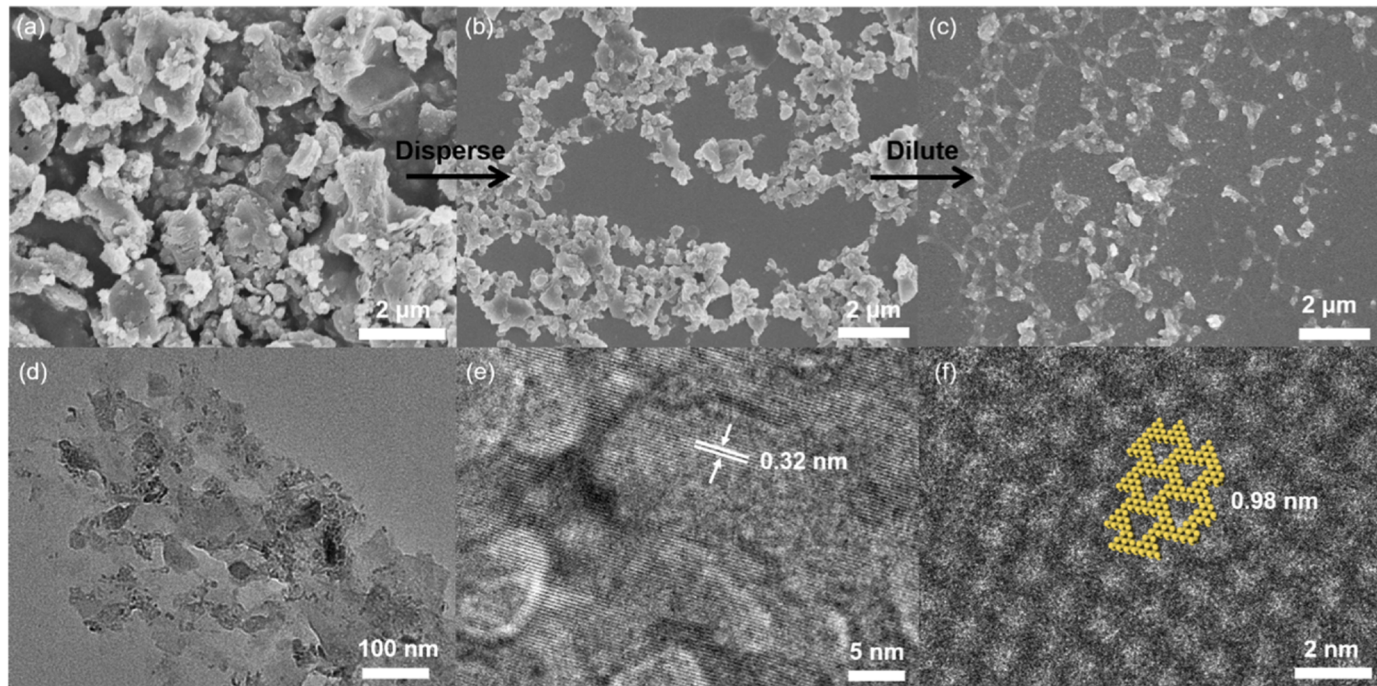


Fig. 3. (a) Contact angle measurements for HCN and BCN. (b) The Zeta potential of BCN and HCN. (c) Particle-size distribution of HCN solution. (d) The XRD patterns of HCN and BCN.



**Fig. 4.** (a) SEM image of HCN solid. (b) SEM image of HCN suspension. (c) SEM image of HCN diluted solution. (d) TEM image of HCN solution. (e-f) HR-TEM images of HCN solution.

observation. The average spacing of periodic lattice fringes is determined to be 0.32 nm, aligning with the (002) facets of HCN (Fig. 4e). The individual crystalline domains are observed in Fig. 4f, which are well-matched with the superimposed structural models. These results confirm that the HCN has a short-range ordered crystalline structure, which agrees with the XRD results. Moreover, the results of the element mapping test indicate a uniform distribution of C, N, and K in the HCN sample (Fig. S10).

### 3.2. Enhanced light absorption and charge separation due to salt-assisted synthesis

To examine the impact of salt-assisted synthesis on catalyst properties, a series of characterizations are conducted. Compared with BCN, the color of the HCN sample transitions from a light-yellow hue to orange-yellow, and the optical absorption edge of the HCN gets red-shifted (Fig. 5a). Based on the Tauc plots, the bandgap of BCN is calculated to be 2.68 eV, while that of HCN is 2.60 eV (Fig. S11). Additionally, the absorption intensity of HCN is significantly higher than that of BCN at both short and long wavelengths, which can be related to the structural differences (Fig. S12). The XPS valence band (VB) spectra are collected to study the band structure of catalysts (Fig. S13). The XPS-VB edges of BCN and HCN are 1.68 and 1.53 eV, approximately. The flat band potential of the catalyst is ascertained through Mott-Schottky tests [43]. In Fig. S14, the flat band potentials of BCN and HCN are examined to be  $-0.12$  and  $-0.25$  V versus reverse hydrogen electrode, respectively. Combining the above results, the VB maximum values are computed to be 1.56 eV for BCN and 1.28 eV for HCN. According to the energy band formula, the corresponding conduction band (CB) minimum positions of HCN and BCN are calculated to be  $-1.32$  and  $-1.12$  eV, respectively. From the band structure of the catalyst (Fig. S15), it is evident that the CB minimum position of HCN shifts towards a more negative potential, suggesting an increased driving force for proton reduction.

Photoluminescence (PL) spectra are then conducted to reveal the separation/transfer of charge carriers in HCN and BCN samples. As shown in Fig. 5b, salt-assisted synthesis significantly reduces the PL

intensity of carbon nitride, confirming that the charge recombination rate is drastically inhibited in the HCN sample [44]. Moreover, the time-resolved PL measurement results (Fig. S16) indicate that the PL decay of HCN (average lifetime of 2.62 ns) is much faster than that of BCN (average lifetime of 5.24 ns), suggesting that the electrons and holes on the HCN surface may participate more quickly in the following redox reactions. Owing to the short lifetime of electrons on the surface of HCN, the electron paramagnetic resonance (EPR) intensity under illumination is also significantly weakened (Fig. S17).

Subsequently, the separation/transfer efficiency of the charge carriers is analyzed by surface photovoltaic spectroscopy (SPV). The positive and negative signals represent the migration of holes and electrons toward the surface [45]. As shown in Fig. 5c, the SPV response intensity of HCN is significantly higher than that of BCN. For the same type of semiconductor, the higher the surface photovoltaic value, the better the photo-generated charge carriers separation efficiency. To examine the dynamic behavior of photo-generated charge carriers, transient-state surface photovoltaic (TPV) is carried out. HCN exhibits a higher photovoltaic response, indicating that more photo-generated charge carriers separate and migrate to the catalyst surface (Fig. 5d) [46]. All the above results confirm that the HCN sample with salt-assisted introduction has better charge transfer performance.

To further elucidate the effect of salt-assisted synthesis on the charge separation/transport properties of catalysts, electrochemical impedance spectroscopy (EIS), photocurrent and linear sweep voltammetry (LSV) measurements are performed. A marked decrease in Nyquist plots diameter for HCN is observed in Fig. 5e, demonstrating that the charge transfer resistance of HCN is much smaller than BCN [47]. As shown in Fig. 5f, HCN exhibits an enhanced photocurrent response, strongly indicating that the transport of photo-generated carriers is promoted [48]. Moreover, the cathodic current density of HCN surpasses that of BCN significantly, signifying superior hydrogen production activity in HCN (Fig. S18). The overpotential of HCN is lower than that of BCN, suggesting stronger surface reducibility of HCN.

To further uncover the mechanism of enhanced light absorption and charge separation properties, the density of states of BCN and HCN is shown in Fig. 6a. Compared with BCN, the conduction band of HCN is

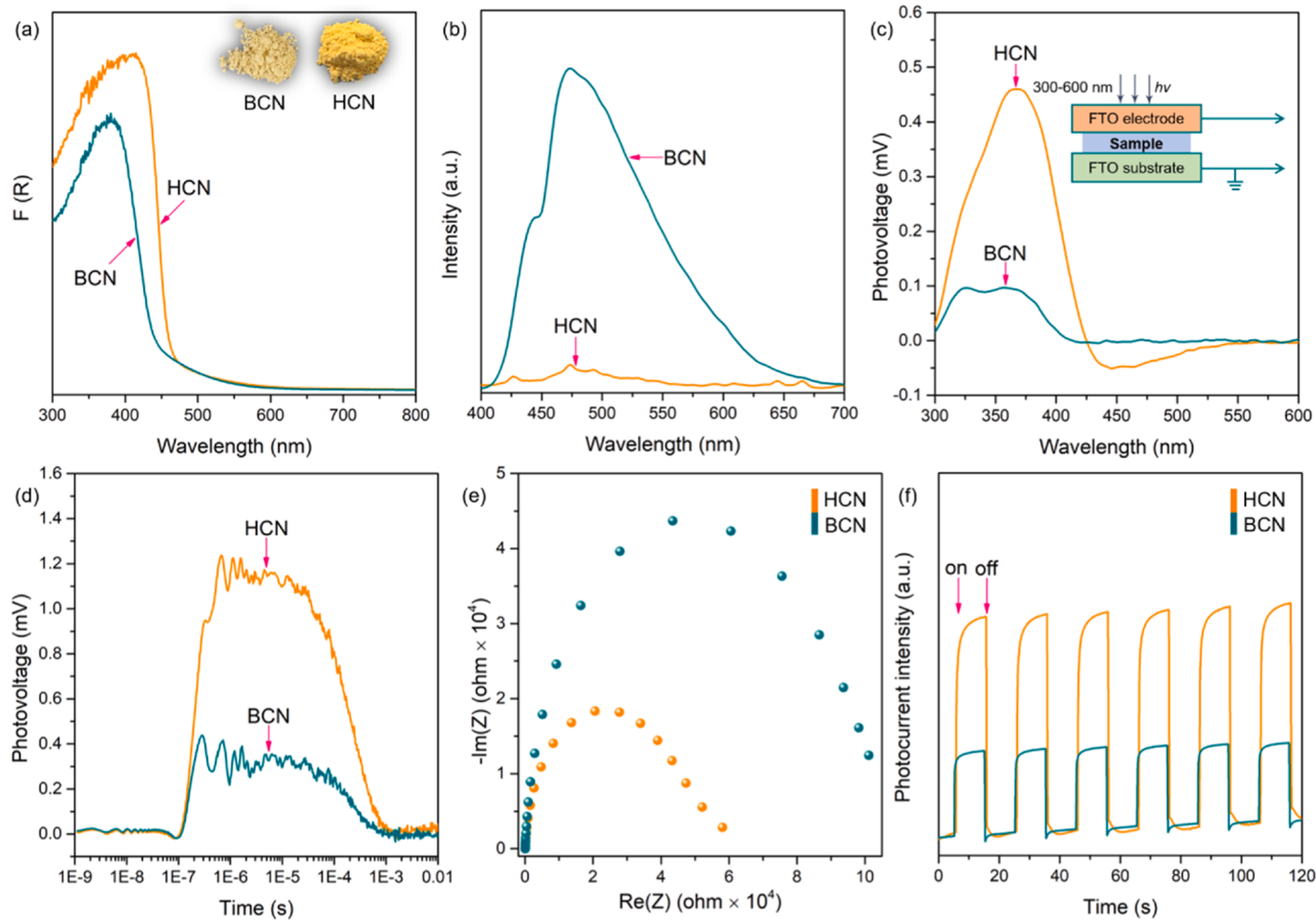


**Fig. 5.** (a) UV-Vis diffuse reflectance spectra of HCN and BCN. Inset: photograph of the samples. (b) PL spectra of HCN and BCN under 380 nm excitation. (c) Steady-state surface photovoltage spectra of HCN and BCN. (d) Transient-state surface photovoltage spectra of HCN and BCN. (e) Electrochemical impedance spectroscopy of HCN and BCN. (f) Transient photocurrents of HCN and BCN.

significantly lowered. The corresponding projected density of states in Fig. 6b, including  $\sigma$ ,  $\pi$  and  $d$  electrons, clearly shows that more  $\sigma$  electron distribution of HCN contributes to the narrowed bandgap, thereby improving the light harvesting of HCN in the visible region. The calculated HOMO and LUMO of BCN in Fig. 6c show a uniform distribution of electrons and holes. In contrast, HCN exhibits an apparent spatial separation between the hole of HOMO and the electron of LUMO (Fig. 6d). The above analysis demonstrates that HCN favors charge separation and light harvesting in the visible region. Considering the enhanced light absorption capacity and improved charge separation efficiency, we speculate that HCN may exhibit better performance in photocatalytic reactions.

### 3.3. Measurement of photocatalytic activity

The hydrogen production reaction is utilized as a probe reaction to investigate the effect of salt-assisted photocatalytic efficiency. The photocatalytic hydrogen production of HCN and BCN is evaluated by loading 3 wt% Pt as a co-catalyst and utilizing triethanolamine as the hole sacrificial agent. As shown in Fig. 7a, the photocatalytic hydrogen evolution rate of BCN is about  $24 \mu\text{mol}\cdot\text{h}^{-1}$ . In contrast, HCN can efficiently catalyze the photocatalytic hydrogen production reaction, and its hydrogen production rate reaches  $392 \mu\text{mol}\cdot\text{h}^{-1}$ , which is a remarkable 16-fold enhancement over BCN, highlighting the advancement of the quasi-homogeneous catalytic system. Notably, the hydrogen evolution rate of HCN even surpasses that of the reported carbon nitrides

when TEOA is used as a sacrificial agent (Table S2). Due to the salt-assisted synthesis, the improved light absorption intensity of HCN samples results in a significantly higher hydrogen production rate under long-wavelength irradiation ( $\lambda > 470 \text{ nm}$ ) compared to BCN (Fig. 7b).

Subsequently, the photocatalytic stability of HCN is tested through multiple-cycle tests. Fig. 7c shows no noticeable deactivation of photocatalytic activity even after four cycle tests, indicating that the HCN sample exhibits excellent photostability. The characterizations after the reaction further demonstrate the stability of the HCN structure. Fig. S19a indicates that the overall FT-IR spectra of HCN remain similar, with only a decrease in peak intensity at  $995$  and  $1150 \text{ cm}^{-1}$  before and after the reaction. XPS results indicate that the content of K element in the HCN structure decreases after the reaction (Fig. S19b), likely due to the cation exchange between HCN and water. Furthermore, it is worth noting that no significant changes in crystal structure are observed (Fig. S20). Therefore, the structure of HCN can be considered relatively stable.

Furthermore, wavelength-dependent apparent quantum yield (AQY) reactions are measured. As displayed in Fig. 7d, AQY is estimated to be 24.1% at  $420 \text{ nm}$  for the HCN sample. Even at  $470 \text{ nm}$  of the absorption band edge, HCN still exhibits an AQY of 4.61%. In contrast, the AQYs of BCN are only 3.88% at  $420 \text{ nm}$  and 1.11% at  $470 \text{ nm}$  (Fig. S21). Notably, the AQY value of hydrogen production is well matched to the light absorption of the sample, indicating that incident photons drive the photocatalytic reaction. These results directly illustrate that the quasi-homogeneous photocatalytic system does have a decisive impact on

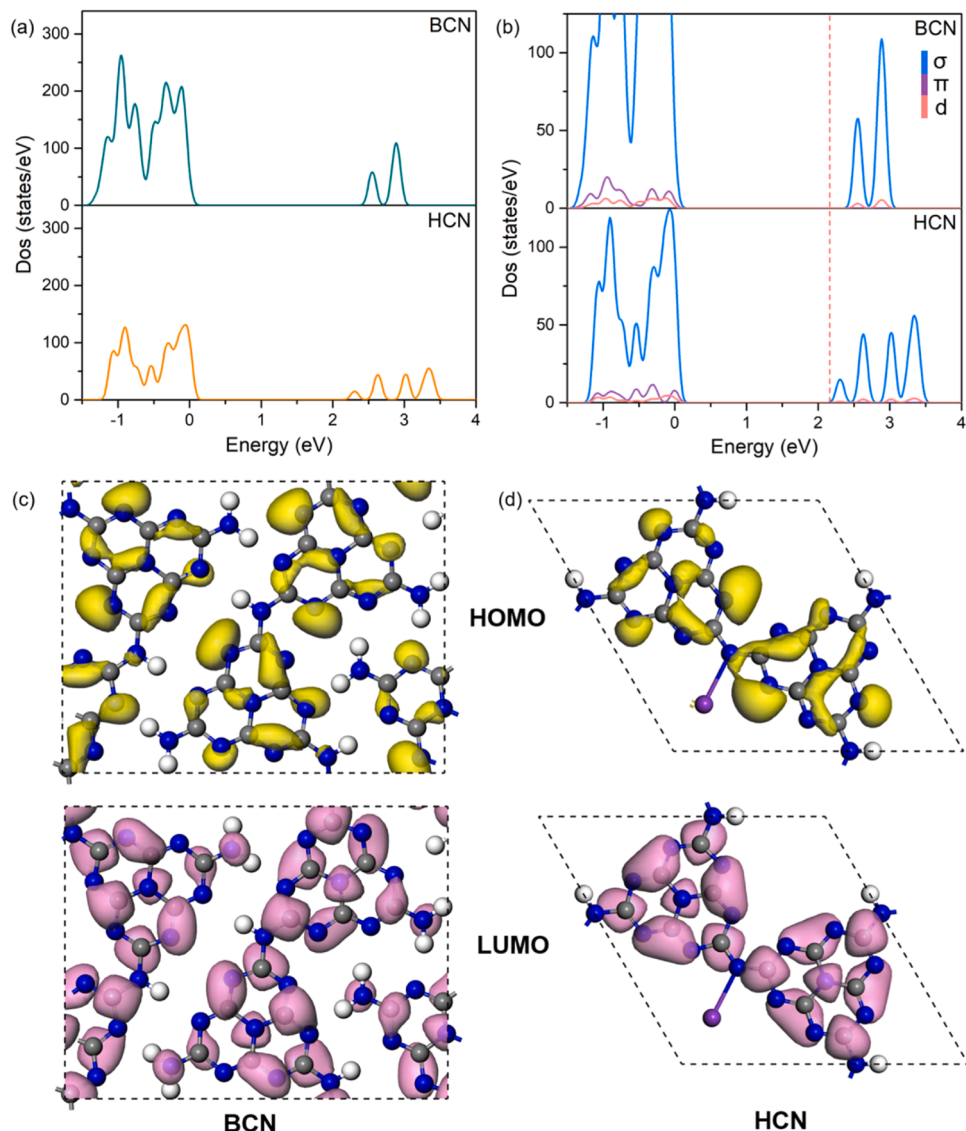


**Fig. 6.** (a) The density of states and (b) projected density of states including  $\sigma$ ,  $\pi$  and  $d$  electrons of BCN and HCN. The calculated spatial distribution of HOMO (yellow) and LUMO (purple) for (c) BCN and (d) HCN. C, N, H and K atoms are denoted with gray, blue, white and purple spheres, respectively.

enhancing hydrogen production efficiency. The mechanism of photocatalytic hydrogen production is shown in Fig. S22 [49–51]. First, HCN is excited by visible light to generate electron-hole pairs. The photogenerated electrons then migrate to the catalyst surface and reduce the adsorbed  $\text{H}^+$  to  $\text{H}_2$ . Likewise, photogenerated holes oxidize the sacrificial agent TEOA.

We further study the photocatalytic activity of HCN for  $\text{H}_2\text{O}_2$  production. The photocatalytic  $\text{H}_2\text{O}_2$  production was performed by dispersing catalyst in a water/isopropanol mixed solution at room temperature in an  $\text{O}_2$  atmosphere. As displayed in Fig. S23, the photocatalytic  $\text{H}_2\text{O}_2$  production rate is estimated to be as high as  $305 \mu\text{mol}\cdot\text{h}^{-1}$  for HCN, which is 13.8 times that of BCN. The significantly improved  $\text{H}_2\text{O}_2$  production of HCN also demonstrates the superiority of this quasi-homogeneous photocatalytic system again. The mechanism of photocatalytic  $\text{H}_2\text{O}_2$  production is shown in Fig. S24a. Photogenerated electrons react with  $\text{H}^+$  and oxygen to generate hydrogen peroxide, and isopropanol is oxidized by photogenerated holes. The fitting results of the rotating disk electrode test show that the average number of transferred electrons is about 1.93, indicating that the process of HCN catalyzing oxygen reduction to generate hydrogen peroxide is mainly a one-step two-electron process (Fig. S24b).

### 3.4. Mechanism and method universality

To clarify the adsorption of molecules on the interface, density functional theory (DFT)-based first-principles calculations were implemented to obtain the binding energies of water molecule at the BCN and HCN interfaces, respectively. The simulated snapshots of the equilibrium position of water molecules at the BCN and HCN interfaces are shown in Figs. 8a and 8b, it can be clearly observed that the HCN interface has a stronger adsorption effect on water molecule than the BCN interface. To further investigate the adsorption mechanism of water molecules on various interfaces, the deformation charge density is further calculated in Fig. S25. Fig. S25a shows that there is a significant overlap between the electron cloud of water molecules and the electron cloud of HCN surface. Additionally, as shown in Fig. S25b, O atom is adsorbed near K atom on the HCN surface that have lost electrons, while there is no apparent adsorption site on the BCN surface (Fig. S25c and S25d). It indicates a strong interaction between the atoms, leading to the stable adsorption of water molecules on the HCN surface.

To demonstrate the universality of this salt-assisted synthesis method, we introduce KCl into the thermal polymerization process for synthesizing carbon nitride materials from other precursors. Through

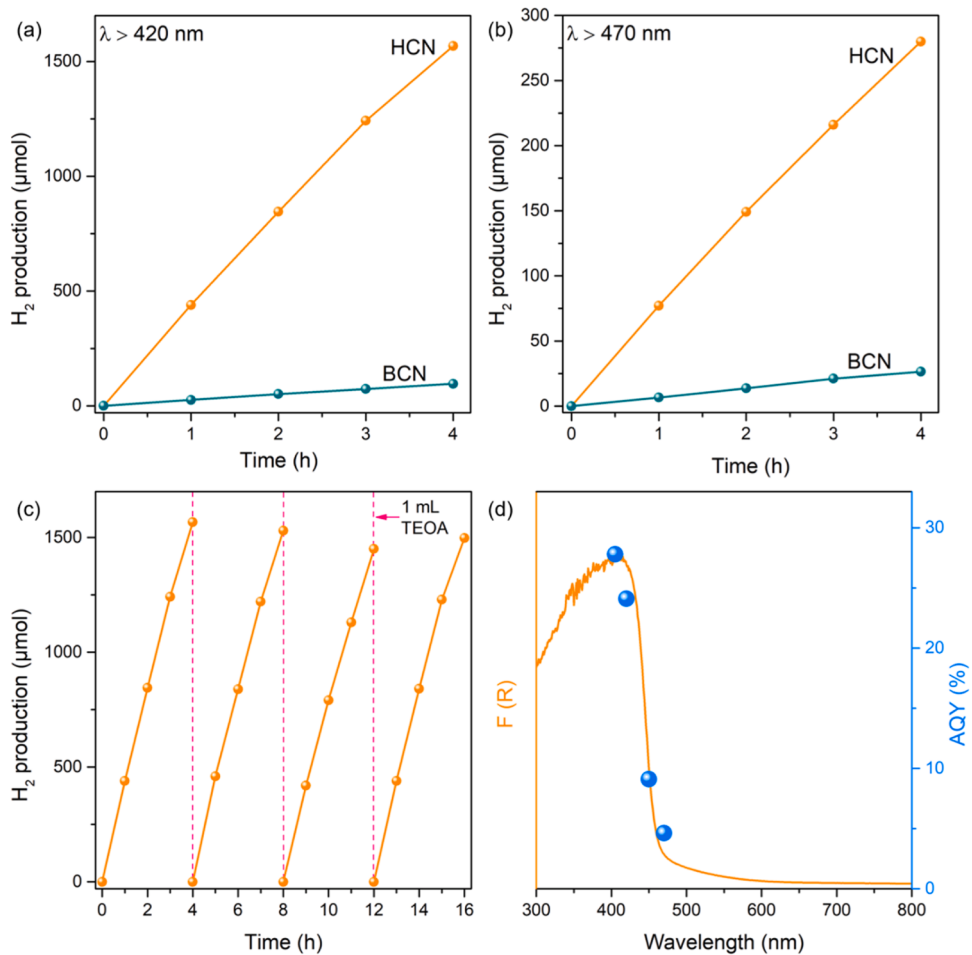


**Fig. 7.** Photocatalytic H<sub>2</sub> production tests of HCN and BCN under visible light irradiation (a)  $\lambda > 420$  nm and (b)  $\lambda > 470$  nm. (c) Time course of H<sub>2</sub> production over HCN ( $\lambda > 420$  nm). (d) Wavelength-dependent AQY of H<sub>2</sub> evolution over HCN (right axis) and UV-Vis diffuse reflectance spectrum of HCN (left axis).

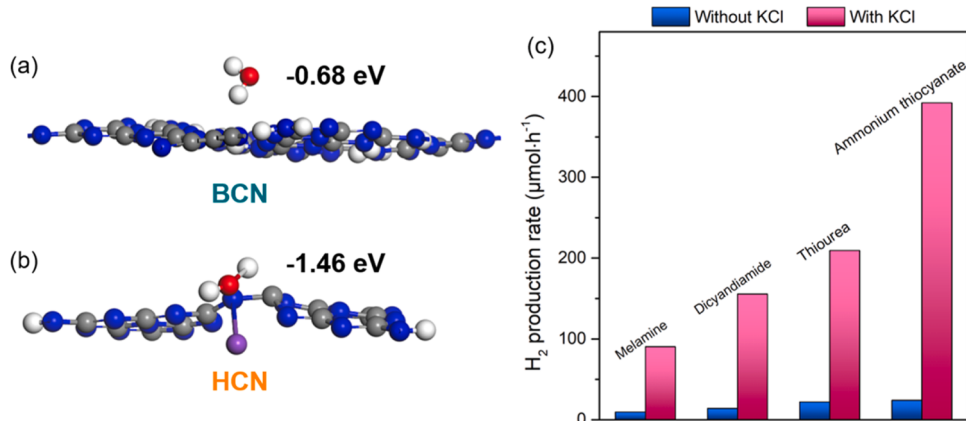


**Fig. 8.** Snapshots of adsorption of water molecule on (a) BCN surface and (b) HCN surface. C, N, H, O and K atoms are denoted with gray, blue, white, red and purple spheres, respectively. (c) The experiments on the universality of salt-assisted synthesis.

XRD testing, it can be concluded that the samples exhibit Potassium Poly (Heptazine Imide) (K-PHI) type crystal structures after the introduction of KCl (Fig. S26) [52]. All these carbon nitride samples involving KCl in synthesis processes exhibit higher photocatalytic hydrogen production activity under visible light irradiation than bulk samples (Fig. 8c). The influence of potassium content in the structure on the photocatalytic activity is also discussed. As shown in Fig. S27, the photocatalytic activity of the material exhibited initial enhancement followed by a

decline with the increase of potassium content. The reason for the decrease in photocatalytic activity may be that the sample contains more potassium chloride that has not been removed, resulting in a reduction in the amount of photocatalyst. In addition, we also compared the effects of different alkali metal salts on photocatalytic activity. Potassium and sodium are equally effective, while lithium is relatively weak (Fig. S28). These results confirm that the salt-assisted synthesis method is an efficient and universal way to prepare high-performance carbon nitride

materials.

#### 4. Conclusion

In summary, a surface and structure functionalized carbon nitride material has been synthesized by the salt-assisted method. The incorporation of hydrophilic groups on the surface enables HCN to disperse well in water, leading to the formation of a quasi-homogeneous catalytic system. Simultaneously, the introduction of potassium ions and changes in crystal structure essentially enhance the separation and transfer efficiency of photo-generated charge carriers. Thus, the as-obtained HCN photocatalyst exhibits a 16-fold enhancement in photocatalytic hydrogen production and a 6-fold increase in apparent quantum efficiency (420 nm) compared to bulk PCN. This research paves a promising approach to improve the intrinsic activity of carbon nitride-based photocatalysts and highlights the critical role of salt-assisted synthesis. Furthermore, the constructed novel quasi-homogeneous catalytic system holds potential for broad applications in other photocatalytic energy/environment reactions, including CO<sub>2</sub> reduction, nitrogen fixation and organic conversion.

#### CRediT authorship contribution statement

**Zequn Wang:** Software. **Chong Wang:** Writing – original draft, Methodology, Investigation, Conceptualization. **Yichun Lu:** Writing – original draft, Investigation, Data curation. **Yusuke Asakura:** Writing – original draft, Investigation, Writing – review & editing. **Yusuke Yamauchi:** Writing – original draft, Conceptualization. **Liwei Wang:** Investigation. **Zhanhui Yuan:** Writing – original draft, Supervision, Resources, Project administration, Conceptualization. **Sameh M. Osman:** Formal analysis, Investigation. **Hongwu Liao:** Investigation. **Weiming Zhou:** Writing – original draft, Investigation. **Yuhe He:** Investigation. **Meng An:** Writing – original draft, Software.

#### Declaration of Competing Interest

The authors declare that they have no known competing financial interests or personal relationships that could have appeared to influence the work reported in this paper.

#### Data availability

Data will be made available on request.

#### Acknowledgments

This work was supported by the Department of Science and Technology of Fujian Province (No. 2022H6021), the Forestry Science and Technology Project of Fujian Province (No. 2023FKJ27), the Youth Innovation Team of Shaanxi Universities (No. 21JP017), the Joint Research Funds of the Department of Science and Technology of Shaanxi Province and Northwestern Polytechnical University (No. 2020GXZH-Z-025), the JST-ERATO Yamauchi Materials Space-Tectonics Project (JPMJER2003), and the UQ-Yonsei International Research Project. This work used the Queensland node of the NCRIS-enabled Australian National Fabrication Facility (ANFF). We express our gratitude for English editing software, such as Grammarly and ChatGPT, for refining language and checking grammatical errors in our manuscript. The authors also extend their appreciation to the Deputyship for Research and Innovation, Ministry of Education in Saudi Arabia for funding this research (IFKSUOR3-615-4).

#### Appendix A. Supporting information

Supplementary data associated with this article can be found in the online version at [doi:10.1016/j.apcatb.2024.123902](https://doi.org/10.1016/j.apcatb.2024.123902).

#### References

- [1] N.S. Lewis, Toward cost-effective solar energy use, *Science* 315 (2007) 798–801.
- [2] D.G. Nocera, On the future of global energy, *Daedalus* 135 (2006) 112–115.
- [3] A. Kumar, P. Daw, D. Milstein, Homogeneous catalysis for sustainable energy: hydrogen and methanol economies, fuels from biomass, and related topics, *Chem. Rev.* 122 (2022) 385–441.
- [4] R.C. Armstrong, C. Wolfram, K.P. de Jong, R. Gross, N.S. Lewis, B. Boardman, A. J. Ragauskas, K. Ehrhardt-Martinez, G. Crabtree, M.V. Ramana, The frontiers of energy, *Nat. Energy* 1 (2016) 15020.
- [5] K. Maeda, K. Teramura, D. Lu, T. Takata, N. Saito, Y. Inoue, K. Domen, Photocatalyst releasing hydrogen from water, *Nature* 440 (2006) 295. <https://www.nature.com/articles/440295a>.
- [6] T. Hisatomi, K. Domen, Reaction systems for solar hydrogen production via water splitting with particulate semiconductor photocatalysts, *Nat. Catal.* 2 (2019) 387–399.
- [7] Q. Wang, K. Domen, Particulate photocatalysts for light-driven water splitting: mechanisms, challenges, and design strategies, *Chem. Rev.* 120 (2020) 919–985.
- [8] Q. Wang, M. Nakabayashi, T. Hisatomi, S. Sun, S. Akiyama, Z. Wang, Z. Pan, X. Xiao, T. Watanabe, T. Yamada, N. Shibata, T. Takata, K. Domen, Oxsulfide photocatalyst for visible-light-driven overall water splitting, *Nat. Mater.* 18 (2019) 827–832.
- [9] S. Chen, T. Takata, K. Domen, Particulate photocatalysts for overall water splitting, *Nat. Rev. Mater.* 2 (2017) 17050. <https://www.nature.com/articles/natrevmats201750>.
- [10] H. Nishiyama, T. Yamada, M. Nakabayashi, Y. Maehara, M. Yamaguchi, Y. Kuromiya, Y. Nagatsuma, H. Tokudome, S. Akiyama, T. Watanabe, R. Narushima, S. Okunaka, N. Shibata, T. Takata, T. Hisatomi, K. Domen, Photocatalytic solar hydrogen production from water on a 100-m<sup>2</sup> scale, *Nature* 598 (2021) 304–307.
- [11] W. Zhou, Z. Wang, H. Huang, Y. Wu, A.A. Alothman, M. Ouladsmane, Y. Yamauchi, X. Xu, M. An, L. Wang, Z. Yuan, Significant enhancement in hydrogen evolution rate of 2D bismuth oxychloride lamellar membrane photocatalyst with cellulose nanofibers, *Chem. Eng. J.* 456 (2023) 140933.
- [12] W. Zhou, Y. Wu, H. Huang, M. Zhang, X. Sun, Z. Wang, F. Zhao, H. Zhang, T. Xie, M. An, L. Wang, Z. Yuan, 2D lamellar membrane with nanochannels synthesized by bottom-up assembly approach for the superior photocatalytic hydrogen evolution, *Rene. Sust. Energ. Rev.* 168 (2022) 112767.
- [13] Y. Zhao, S. Zhang, R. Shi, G.I.N. Waterhouse, J. Tang, T. Zhang, Two-dimensional photocatalyst design: a critical review of recent experimental and computational advances, *Mater. Today* 34 (2020) 78–91.
- [14] Y. Xiao, G. Tian, W. Li, Y. Xie, B. Jiang, C. Tian, D. Zhao, H. Fu, Molecule self-assembly synthesis of porous few-layer carbon nitride for highly efficient photoredox catalysis, *J. Am. Chem. Soc.* 141 (2019) 2508–2515.
- [15] X. Wang, K. Maeda, A. Thomas, K. Takanabe, G. Xin, J.M. Carlsson, K. Domen, M. Antonietti, A metal-free polymeric photocatalyst for hydrogen production from water under visible light, *Nat. Mater.* 8 (2009) 76–80.
- [16] S. Cao, J. Low, J. Yu, M. Jaroniec, Polymeric photocatalysts based on graphitic carbon nitride, *Adv. Mater.* 27 (2015) 2150–2176.
- [17] Y. Zheng, L. Lin, B. Wang, X. Wang, Graphitic carbon nitride polymers toward sustainable photoredox catalysis, *Angew. Chem. Int. Ed.* 54 (2015) 12868–12884.
- [18] F.K. Kessler, Y. Zheng, D. Schwarz, C. Merschjann, W. Schnick, X. Wang, M. J. Bojdys, Functional carbon nitride materials - design strategies for electrochemical devices, *Nat. Rev. Mater.* 2 (2017) 17030. <https://www.nature.com/articles/natrevmats201730>.
- [19] Y. Zhang, Z. Zhou, Y. Shen, Q. Zhou, J. Wang, A. Liu, S. Liu, Y. Zhang, Reversible assembly of graphitic carbon nitride 3D network for highly selective dyes absorption and regeneration, *ACS Nano* 10 (2016) 9036–9043.
- [20] S. Guo, Z. Deng, M. Li, B. Jiang, C. Tian, Q. Pan, H. Fu, Phosphorus-doped carbon nitride tubes with a layered micro-nanostructure for enhanced visible-light photocatalytic hydrogen evolution, *Angew. Chem. Int. Ed.* 55 (2016) 1830–1834.
- [21] Z. Lin, X. Wang, Nanostructure engineering and doping of conjugated carbon nitride semiconductors for hydrogen photosynthesis, *Angew. Chem. Int. Ed.* 52 (2013) 1735–1738.
- [22] Y. Xu, C. Qiu, X. Fan, Y. Xiao, G. Zhang, K. Yu, H. Ju, X. Ling, Y. Zhu, C. Su, K<sup>+</sup>-induced crystallization of polymeric carbon nitride to boost its photocatalytic activity for H<sub>2</sub> evolution and hydrogenation of alkenes, *Appl. Catal., B* 268 (2020) 118457.
- [23] A.J. Rieth, Y. Qin, B.C.M. Martindale, D.G. Nocera, Long-lived triplet excited state in a heterogeneous modified carbon nitride photocatalyst, *J. Am. Chem. Soc.* 143 (2021) 4646–4652.
- [24] J. Ji, J. Wen, Y. Shen, Y. Lv, Y. Chen, S. Liu, H. Ma, Y. Zhang, Simultaneous noncovalent modification and exfoliation of 2D carbon nitride for enhanced electrochemiluminescent biosensing, *J. Am. Chem. Soc.* 139 (2017) 11698–11701.
- [25] H. Che, X. Gao, J. Chen, J. Hou, Y. Ao, P. Wang, Iodide-induced fragmentation of polymerized hydrophilic carbon nitride for high-performance quasi-homogeneous photocatalytic H<sub>2</sub>O<sub>2</sub> production, *Angew. Chem. Int. Ed.* 60 (2021) 25546–25550.
- [26] C. Huang, J. Wen, Y. Shen, F. He, L. Mi, Z. Gan, J. Ma, S. Liu, H. Ma, Y. Zhang, Dissolution and homogeneous photocatalysis of polymeric carbon nitride, *Chem. Sci.* 9 (2018) 7912–7915.
- [27] J. Zhang, M. Zhang, L. Lin, X. Wang, Sol processing of conjugated carbon nitride powders for thin-film fabrication, *Angew. Chem. Int. Ed.* 54 (2015) 6297–6301.
- [28] I. Krivtsov, D. Mitoraj, C. Adler, M. Ilkaeva, M. Sardo, L. Mafra, C. Neumann, A. Turchanin, C. Li, B. Dietzek, R. Leiter, J. Biskupek, U. Kaiser, C. Im, B. Kirchhoff, T. Jacob, R. Beranek, Water-soluble polymeric carbon nitride colloidal

nanoparticles for highly selective quasi-homogeneous photocatalysis, *Angew. Chem. Int. Ed.* 59 (2020) 487–495.

[29] D. Zhang, X. Han, T. Dong, X. Guo, C. Song, Z. Zhao, Promoting effect of cyano groups attached on  $\text{g-C}_3\text{N}_4$  nanosheets towards molecular oxygen activation for visible light-driven aerobic coupling of amines to imines, *J. Catal.* 366 (2018) 237–244.

[30] G. Li, Z. Xie, S. Chai, X. Chen, X. Wang, A facile one-step fabrication of holey carbon nitride nanosheets for visible-light-driven hydrogen evolution, *Appl. Catal., B* 283 (2021) 119637.

[31] J. Kröger, F. Podjaski, G. Savasci, I. Moudrakovski, A. Jiménez-Solano, M. W. Terban, S. Bette, V. Duppel, M. Joos, A. Senocrate, R. Dinnebier, C. Ochsnerfeld, B.V. Lotsch, Conductivity Mechanism in Ionic 2D Carbon Nitrides: From Hydrated Ion Motion to Enhanced Photocatalysis, *Adv. Mater.* 34 (7) (2022) 2107061. <https://onlinelibrary.wiley.com/doi/10.1002/adma.202107061>.

[32] Z. Chen, S. Pronkin, T.-P. Fellinger, K. Kailasam, G. Vilé, D. Albani, F. Krumeich, R. Leary, J. Barnard, J.M. Thomas, J. Pérez-Ramírez, M. Antonietti, D. Dontsova, Merging single-atom-dispersed silver and carbon nitride to a joint electronic system via copolymerization with silver tricyanomethanide, *ACS Nano* 10 (2016) 3166–3175.

[33] C. Wang, Y. Hou, J. Cheng, M.-J. Lin, X. Wang, Biomimetic donor-acceptor motifs in carbon nitrides: enhancing red-light photocatalytic selective oxidation by rational surface engineering, *Appl. Catal., B* 294 (2021) 120259.

[34] C. Wang, Q. Wan, J. Cheng, S. Lin, A. Savateev, M. Antonietti, X. Wang, Efficient aerobic oxidation of alcohols to esters by acidified carbon nitride photocatalysts, *J. Catal.* 393 (2021) 116–125.

[35] L. Lin, H. Ou, Y. Zhang, X. Wang, Tri-s-triazine-based crystalline graphitic carbon nitrides for highly efficient hydrogen evolution photocatalysis, *ACS Catal.* 6 (2016) 3921–3931.

[36] H. Yu, R. Shi, Y. Zhao, T. Bian, Y. Zhao, C. Zhou, G.I.N. Waterhouse, L.-Z. Wu, C.-H. Tung, T. Zhang, Alkali-assisted synthesis of nitrogen deficient graphitic carbon nitride with tunable band structures for efficient visible-light-driven hydrogen evolution, *Adv. Mater.* 29 (16) (2017) 1605148. <https://onlinelibrary.wiley.com/doi/10.1002/adma.201605148>.

[37] P. Yang, H. Ou, Y. Fang, X. Wang, A facile steam reforming strategy to delaminate layered carbon nitride semiconductors for photoredox catalysis, *Angew. Chem. Int. Ed.* 56 (2017) 3992–3996.

[38] H. Tan, X. Gu, P. Kong, Z. Lian, B. Li, Z. Zheng, Cyano group modified carbon nitride with enhanced photoactivity for selective oxidation of benzylamine, *Appl. Catal., B* 242 (2019) 67–75.

[39] J. Li, D. Wu, J. Iocozzia, H. Du, X. Liu, Y. Yuan, W. Zhou, Z. Li, Z. Xue, Z. Lin, Achieving efficient incorporation of  $\pi$ -electrons into graphitic carbon nitride for markedly improved hydrogen generation, *Angew. Chem. Int. Ed.* 58 (2019) 1985–1989.

[40] Y. Wang, M.K. Bayazit, S.J.A. Moniz, Q. Ruan, C.C. Lau, N. Martsinovich, J. Tang, Linker-controlled polymeric photocatalyst for highly efficient hydrogen evolution from water, *Energy Environ. Sci.* 10 (2017) 1643–1651.

[41] Y. Li, P. Li, J. Wang, Y. Yang, W. Yao, Z. Wei, J. Wu, X. Yan, X. Xu, Y. Liu, Y. Zhu, Water soluble graphitic carbon nitride with tunable fluorescence for boosting broad-response photocatalysis, *Appl. Catal., B* 225 (2018) 519–529.

[42] J. Kröger, A. Jiménez-Solano, G. Savasci, V.Wh Lau, V. Duppel, I. Moudrakovski, K. Küster, T. Scholz, A. Gouder, M.-L. Schreiber, F. Podjaski, C. Ochsnerfeld, B. V. Lotsch, Morphology control in 2D carbon nitrides: impact of particle size on optoelectronic properties and photocatalysis, *Adv. Funct. Mater.* 31 (28) (2021) 2102468. <https://onlinelibrary.wiley.com/doi/10.1002/adfm.202102468>.

[43] C. Wang, H. Xiao, Y. Lu, J. Lv, Z. Yuan, J. Cheng, Regulation of polymerization kinetics to improve crystallinity of carbon nitride for photocatalytic reactions, *ChemSusChem* 16 (16) (2023) e202300361. <https://chemistry-europe.onlinelibrary.wiley.com/doi/10.1002/cssc.202300361>.

[44] B. Xia, B. He, J. Zhang, L. Li, Y. Zhang, J. Yu, J. Ran, S.-Z. Qiao,  $\text{TiO}_2/\text{FePS}_3$  S-scheme heterojunction for greatly raised photocatalytic hydrogen evolution, *Adv. Energy Mater.* 12 (46) (2022) 2201449. <https://onlinelibrary.wiley.com/doi/10.1002/aenm.202201449>.

[45] X. Ruan, X. Cui, Y. Cui, X. Fan, Z. Li, T. Xie, K. Ba, G. Jia, H. Zhang, L. Zhang, W. Zhang, X. Zhao, J. Leng, S. Jin, D.J. Singh, W. Zheng, Favorable energy band alignment of  $\text{TiO}_2$  anatase/rutile heterophase homojunctions yields photocatalytic hydrogen evolution with quantum efficiency exceeding 45.6%, *Adv. Energy Mater.* 12 (16) (2022) 2200298. <https://onlinelibrary.wiley.com/doi/10.1002/aenm.202200298>.

[46] Y. Zhao, P. Zhang, Z. Yang, L. Li, J. Gao, S. Chen, T. Xie, C. Diao, S. Xi, B. Xiao, C. Hu, W. Choi, Mechanistic analysis of multiple processes controlling solar-driven  $\text{H}_2\text{O}_2$  synthesis using engineered polymeric carbon nitride, *Nat. Commun.* 12 (2021) 3701. <https://www.nature.com/articles/s41467-021-24048-1>.

[47] W. Wang, L. Du, R. Xia, R. Liang, T. Zhou, H.K. Lee, Z. Yan, H. Luo, C. Shang, D. L. Phillips, Z. Guo, In situ protonated-phosphorus interstitial doping induces long-lived shallow charge trapping in porous  $\text{C}_{3-x}\text{N}_4$  photocatalysts for highly efficient  $\text{H}_2$  generation, *Energy Environ. Sci.* 16 (2023) 460–472.

[48] P. Zhang, D. Sun, A. Cho, S. Weon, S. Lee, J. Lee, J.W. Han, D.-P. Kim, W. Choi, Modified carbon nitride nanomaze as bifunctional glucose oxidase-peroxidase for metal-free bioinspired cascade photocatalysis, *Nat. Commun.* 10 (2019) 940. <https://www.nature.com/articles/s41467-019-08731-y>.

[49] W. Huang, Z. Li, C. Wu, H. Zhang, J. Sun, Q. Li, Delaminating  $\text{Ti}_3\text{C}_2$  MXene by blossom of  $\text{ZnIn}_2\text{S}_4$  microflowers for noble-metal-free photocatalytic hydrogen production, *J. Mater. Sci. Technol.* 120 (2022) 89–98.

[50] C. Wu, W. Huang, H. Liu, K. Lv, Q. Li, Insight into synergistic effect of  $\text{Ti}_3\text{C}_2$  MXene and  $\text{MoS}_2$  on anti-photocorrosion and photocatalytic of  $\text{CdS}$  for hydrogen production, *Appl. Catal., B* 330 (2023) 122653.

[51] C. Wu, K. Lv, X. Li, Q. Li, Dual cocatalysts for photocatalytic hydrogen evolution: categories, synthesis, and design considerations, *Chin. J. Catal.* 54 (2023) 137–160.

[52] A. Savateev, N.V. Tarakina, V. Strauss, T. Hussain, K. ten Brummelhuis, J. M. Sánchez Vadillo, Y. Markushyna, S. Mazzanti, A.P. Tyutyunnik, R. Walczak, M. Oschatz, D.M. Guldi, A. Karton, M. Antonietti, Potassium poly(Heptazine Imide): transition metal-free solid-state triplet sensitizer in cascade energy transfer and [3+2]-cycloadditions, *Angew. Chem. Int. Ed.* 59 (2020) 15061–15068.